

Mantle Phase Changes Detected from Stochastic Tomography

Vernon F. Cormier¹, Carolina Lithgow-Bertollini², Lars Stixrude³, and Yingcai Zheng⁴

¹University of Connecticut

²University of California, Los Angeles

³University of California Los Angeles

⁴University of Houston

November 24, 2022

Abstract

Stochastic tomography, made possible by dense deployments of seismic sensors, is used to identify previously undetected and poorly detected changes in the composition and mineral structure of Earth's mantle. This technique inverts the spatial coherence of amplitudes and travel times of body waves to determine the depth and lateral dependence of the spatial spectrum of seismic velocity. The inverted spectrum is interpreted using predictions from the thermodynamic stability of different compositions and mineral phases as a function of temperature and pressure, in which the metamorphic temperature derivative of seismic velocities can be used as a proxy for the effects of heterogeneity induced in a region undergoing a phase change. Peaks in the metamorphic derivative of seismic velocity are found to closely match those found from applying stochastic tomography to elements of Earthscope and FLEX arrays. Within ± 12 km, peaks in the fluctuation of P velocity at 425, 500, and 600 km depth beneath the western US agree those predicted by a mechanical mixture of harzburgite and basalt in a cooler mantle transition zone. A smaller peak at 250 km depth may be associated with chemical heterogeneity induced by dehydration of subducted oceanic sediments, and a peak at 775 km depth with a phase change in subducted basalt. Non-detection of a predicted endothermic phase change near 660 km is consistent with its width being much less than 10 km. These interpretations of the heterogeneity spectrum are consistent with the known history of plate subduction beneath North America.

Mantle Phase Changes Detected from Stochastic Tomography

Vernon F. Cormier¹, Carolina Lithgow-Bertelloni², Lars Stixrude², and Yingcai Zheng³

¹Department of Physics, University of Connecticut

²Department of Earth and Planetary Sciences, University of California, Los Angeles

³Department of Earth and Atmospheric Sciences, University of Houston

Corresponding author: Vernon Cormier (vernon.cormier@uconn.edu)

†Vernon F. Cormier, Department of Physics, University of Connecticut, 196A Auditorium Road, Storrs, CT 06269-3046

Index terms: 7208, 7203, 7260, 3611, 3612

Key Points:

- Stochastic tomography can capture higher order phase and chemical changes undetectable from reflection imaging.
- The heterogeneity spectrum of the upper mantle is marked by peaks associated with depth regions undergoing phase or compositional change.
- The upper mantle beneath the western US is consistent with a history of subduction and slab stagnation in the transition zone.

Abstract

Stochastic tomography, made possible by dense deployments of seismic sensors, is used to identify previously undetected and poorly detected changes in the composition and mineral structure of Earth's mantle. This technique inverts the spatial coherence of amplitudes and travel times of body waves to determine the depth and lateral dependence of the spatial spectrum of seismic velocity. The inverted spectrum is interpreted using predictions from the thermodynamic stability of different compositions and mineral phases as a function of temperature and pressure, in which the metamorphic temperature derivative of seismic velocities can be used as a proxy for the effects of heterogeneity induced in a region undergoing a phase change. Peaks in the temperature derivative of seismic velocity are found to closely match those found from applying stochastic tomography to elements of Earthscope and FLEX arrays. Within ± 12 km, peaks in the fluctuation of P velocity at 425, 500, and 600 km depth beneath the western US agree those predicted by a mechanical mixture of harzburgite and basalt in a cooler mantle transition zone. A smaller peak at 250 km depth may be associated with chemical heterogeneity induced by dehydration of subducted oceanic sediments, and a peak at 775 km depth with a phase change in subducted basalt. Non-detection of a predicted endothermic phase change near 660 km is consistent with its width being much less than 10 km. These interpretations of the heterogeneity spectrum are consistent with the known history of plate subduction beneath North America.

43

Plain Language Summary

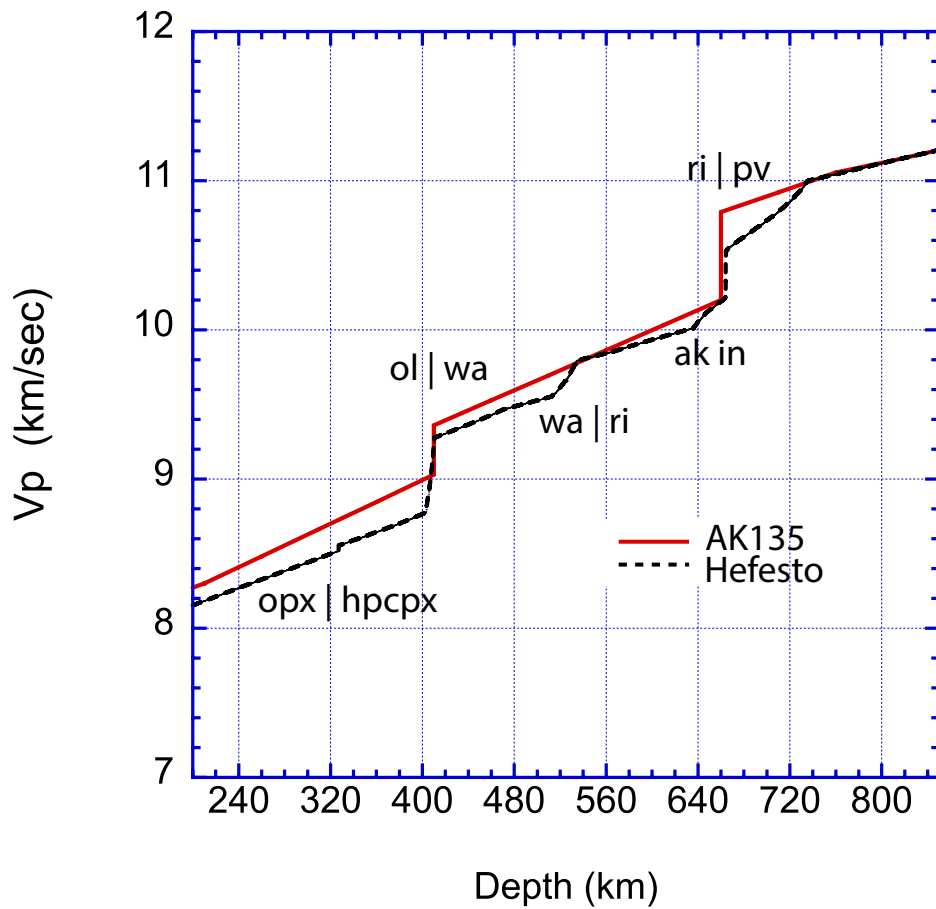
Fluctuations in amplitude and traveltimes of seismic P waves from deep earthquakes observed at

46 the US Array of seismic stations are inverted for a depth dependent spectrum of the intensity of P
47 wave velocity fluctuations. Peaks with depth of this spectrum correlate with the depths predicted
48 for changes in the arrangements of atoms of the silicate minerals comprising the upper 1000 km
49 of Earth's mantle. The structure of the peaks agrees with the known history of tectonic plate
50 subduction beneath the western US.

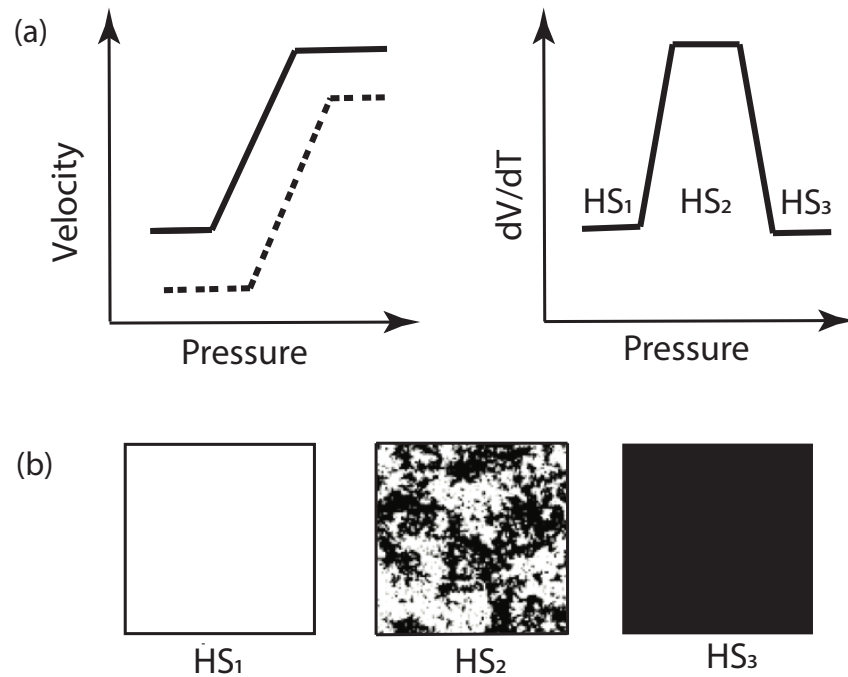
51 **1 Introduction**

52 The best-known solid phase changes in Earth's silicate mantle are commonly detected from the
53 reflection and conversion of body waves interacting with rapid, near discontinuous, changes in
54 velocity and density occurring at or near 410 and 660 km depth (e.g., *Shearer, 1991; Niu et al.,*
55 *2005*). These phase changes also produce multi-pathed body waveforms between 15° -35° great
56 circle range (e.g., *Burdick and Helmberger, 1978; Chu et al., 2012*). The steepness of the inferred
57 P and S velocity gradients between 410 and 660 km in reference Earth models, however, cannot
58 be explained by plausible silicate mantle chemistry without the existence of at least one more
59 phase change between 410 and 660 km. When the tools of mineral physics are applied to a
60 constrained composition of the Earth's mantle, up to two additional phase changes are predicted
61 to occur between the 410 to 660 km. Several other phase changes are also predicted above and
62 below this zone, each having a unique behavior in their Clapeyron slope and the widths in depth
63 over which each occurs (Fig. 1a). The widths of more than half of these are on the order of 15 to
64 60 km, making it difficult to detect them from reflected and converted body waves having
65 similar or shorter wavelengths. A serendipitous seismological discovery from the inversion of P
66 wave coherences across the USArray (*Cormier et al., 2020*) reveals that many these phase
67 changes are marked by peaks in the depth-dependency of the mantle heterogeneity spectrum that
68 correlate with peaks in the temperature derivatives of seismic velocities predicted by
69 thermodynamic models of mantle composition and phase. *Stixrude and Lithgow-Bertelloni*

70 (2005 2007) have demonstrated that small lateral variations in temperature ($<150^\circ\text{K}$) allow the
71 peaks in the predicted temperature derivatives to capture the depth zone in which two competing
72 mineral phases may coexist that are capable of scattering seismic body waves (Fig.2). These peaks
73 in the metamorphic component of the temperature derivatives can be used to identify and
74 interpret peaks in narrow depth ranges of the mantle heterogeneity spectrum. This
75 heterospectrum can be inverted from fluctuations in travel time and amplitudes of seismic waves
76 observed across dense networks of seismic stations by a process known as stochastic
77 tomography. In this paper, our objective is to interpret the seismological results from stochastic
78 tomography applied to seismic arrays located in the western US (Cormier et al., 2020) using the
79 predictions of the thermodynamic code Hefesto (Stixrude and Lithgow-Bertelloni, 2005, 2007)
80 for the temperature derivatives of the P wave velocity. We assume mantle models of both
81 equilibrium pyrolyte and mechanical mixtures of harzburgite and basalt, and examine the effects
82 of temperature and subduction. Before we begin interpretations in section 4, we review the
83 principles and assumptions of stochastic tomography in section 2. In section 3 we discuss the
84 filtering and depth averaging of the metamorphic temperature derivatives predicted by Hefesto
85 required to match the sensitivity achievable with stochastic tomography. Readers primarily
86 interested in our interpretation of the detected phase changes may best begin by reading sections 4
87 and 5, which focus on the interpretation of our results, referring as needed, to the methods of
88 inversion and analysis in sections 2 and 3.



89
 90 **Figure 1.** Dashed black line: P velocity of the upper mantle predicted by the thermodynamic
 91 modeling code Hefesto for a pyrolite composition along a 1600° K isentrope. Red solid line: P
 92 velocity of the AK135 model (Montagner and Kennett, 1995). Sharp, near vertical changes in
 93 slope occur for phase changes at 410 km and 660 km. Milder changes in slope predicted by
 94 Hefesto denote phase changes that occur over broader regions of depth. (Note: The generally
 95 slower Hefesto P velocities shown here, compared to a reference Earth model, are due to an
 96 average Earth geotherm cooler than the assumed 1600° K isentrope in the conductive zone near
 97 Earth's surface and cool perturbations due to slab stagnations in the transition zone (section 4).)
 98



99
 100 **Figure 2.** (a) Illustration of how a change in velocity over a zone of exothermic phase change
 101 affects its temperature derivative assuming a positive Clapeyron slope. Upper left: the solid line
 102 is the velocity change at lower temperature and the dotted line is the velocity change at higher
 103 temperature. Upper right: computed difference derivative of velocity with respect to temperature.
 104 (b) Realizations of the how the heterospectrum may change with depth across a phase change.
 105 The example shown here is inspired by Ising models of electron spin statistics for a
 106 ferromagnetic transition (Blundell and Blundell, 2014).

107 2 Stochastic Tomography

108 2.1 Theory and data

109 Small-scale heterogeneities, unresolvable by conventional tomography, have detectable
 110 signatures in the fluctuation of amplitudes and travel times observed across seismic arrays.
 111 Numerical simulations have shown that small-scale heterogeneity in the upper mantle can affect
 112 the wavefront of an incident teleseismic wave beneath an array. Small differences in the angle of
 113 approach of wavefronts, on the order of a several degrees or less, can produce unique signatures

114 in amplitude and phase fluctuations due to differences in the sensitivity of the wavefronts to the
 115 small-scale structure (e.g., Zheng & Wu 2008; Tkalčić et al., 2010). Measurement of these
 116 fluctuations between array elements can be exploited to invert for the spectrum of heterogeneity
 117 beneath the array with techniques that have been named stochastic tomography (Wu & Flatté,
 118 1990; Wu & Xie, 1991, Zheng & Wu, 2008).

119

120 Transmission fluctuation coherence measurements (eqs. 1a-d) are the starting point for stochastic
 121 tomography. We consider the recorded fields due to two plane waves, PW1 and PW2. We use
 122 $U_1(x_1)$ for the recorded field at x_1 for PW1. Likewise, we use $U_2(x_2)$ for the recorded field at x_2
 123 for PW2. Both fields propagate through the same heterogeneous medium. We also consider their
 124 corresponding reference fields (no heterogeneities), $U_{1ref}(x_1)$ and $U_{2ref}(x_2)$, respectively. We
 125 can write the seismic fields in amplitude and phase terms, for example, $U_1 = u_1 \exp[i\omega t] =$
 126 $u_1 \exp[i\phi]$ and $U_{1ref} = u_{1ref} \exp[i\omega t_{ref}] = u_{1ref} \exp[i\phi_{ref}]$. Similar representations are
 127 applied to PW2. A Rytov approximation provides the relationship between the scattered field and
 128 the reference field: $U_1 = U_{1ref} e^{\psi_1}$. The complex function ψ has a real part, which is the
 129 logarithmic amplitude, and an imaginary part, which is the phase (or travelttime) difference with
 130 respect to the reference value. In our work, the observables are the ratios of log amplitude and
 131 travel time differences (eqs. 1c-d) from those computed in a reference Earth model. Transverse
 132 coherence functions are constructed as a function of the lag distance x between pairs of
 133 receivers. The brace brackets in eqs. 1a-b, define the logarithmic amplitude $\langle u_1 u_2 \rangle$ and $\langle \phi_1 \phi_2 \rangle$
 134 phase coherences by averaging measurements for a specific lag distance over all combinations of
 135 two receivers in an array separated by that lag distance. Non-dimensional coherence values
 136 range from zero (amplitude and travelttime fluctuations) at neighboring receivers to 1 for perfect
 137 correlation of amplitudes and to 2π for perfect correlation of phase.

138

$$\begin{aligned}
(1a) \quad & \langle u_1 u_2 \rangle = \frac{1}{2} \operatorname{Re} \langle \psi_1 \psi_2^* \rangle + \frac{1}{2} \operatorname{Re} \langle \psi_1 \psi_2 \rangle \\
(1b) \quad & \langle \phi_1 \phi_2 \rangle = \frac{1}{2} \operatorname{Re} \langle \psi_1 \psi_2^* \rangle - \frac{1}{2} \operatorname{Re} \langle \psi_1 \psi_2 \rangle, \quad \text{where} \\
(1c) \quad & \psi(\omega) = \ln(u / u_{\text{ref}}) + i\omega(t - t_{\text{ref}}) \\
(1d) \quad & u = \frac{\psi + \psi^*}{2} \quad \text{and} \quad \phi = \frac{\psi - \psi^*}{2i}
\end{aligned}$$

139

140

141 To construct the complex functions $\psi(\omega)$, we measure u and u_{ref} from observed and synthetic
 142 seismograms around the direct P waves from the outputs of a multi-taper filter at 0.7 Hz, and
 143 measure the traveltime difference $t - t_{\text{ref}}$ from cross-correlation of observed and predicted
 144 reference waveforms.

145

146 Stochastic tomography assumes that the functional behaviors of the coherences with lag distance
 147 are due to the interference of plane waves scattered by random heterogeneities having an
 148 unknown power spectrum as a function of wavenumber and depth. The transverse coherences
 149 can be written as an integral over horizontal wavenumber and depth, with an integrand
 150 containing the power spectrum (eqs. 2a-c).

151

$$(2a) \quad \langle u_1 u_2 \rangle = (2\pi)^{-1} \int_0^H d\xi a_1(\xi) a_2(\xi) \int_0^\infty J_0[(\kappa R(\xi))] \sin[\omega\theta_1(\xi)] \sin[\omega\theta_2(\xi)] P(\xi, \kappa) \kappa d\kappa$$

$$(2b) \quad \langle \phi_1 \phi_2 \rangle = (2\pi)^{-1} \int_0^H d\xi a_1(\xi) a_2(\xi) \int_0^\infty J_0[(\kappa R(\xi))] \cos[\omega\theta_1(\xi)] \cos[\omega\theta_2(\xi)] P(\xi, \kappa) \kappa d\kappa$$

$$(2c) \quad \langle u_1 \phi_2 \rangle = (2\pi)^{-1} \int_0^H d\xi a_1(\xi) a_2(\xi) \int_0^\infty J_0[(\kappa R(\xi))] \sin[\omega\theta_1(\xi)] \cos[\omega\theta_2(\xi)] P(\xi, \kappa) \kappa d\kappa$$

153

154 In eqs. 2a-c, P is the power spectrum as a function of depth ξ and horizontal wavenumber κ .
 155 H is the thickness of a heterogeneous layer. Functions a_1, a_2, θ_1 , and θ_2 are defined in Cormier et
 156 al. (2020). The function R appearing in the argument of the Bessel function J_0 is the horizontal
 157 distance between the pair of rays arriving at a specific lag distance at depth ξ . The average sum
 158 of a coherence measurement at each lag from many sources at different distances and azimuths

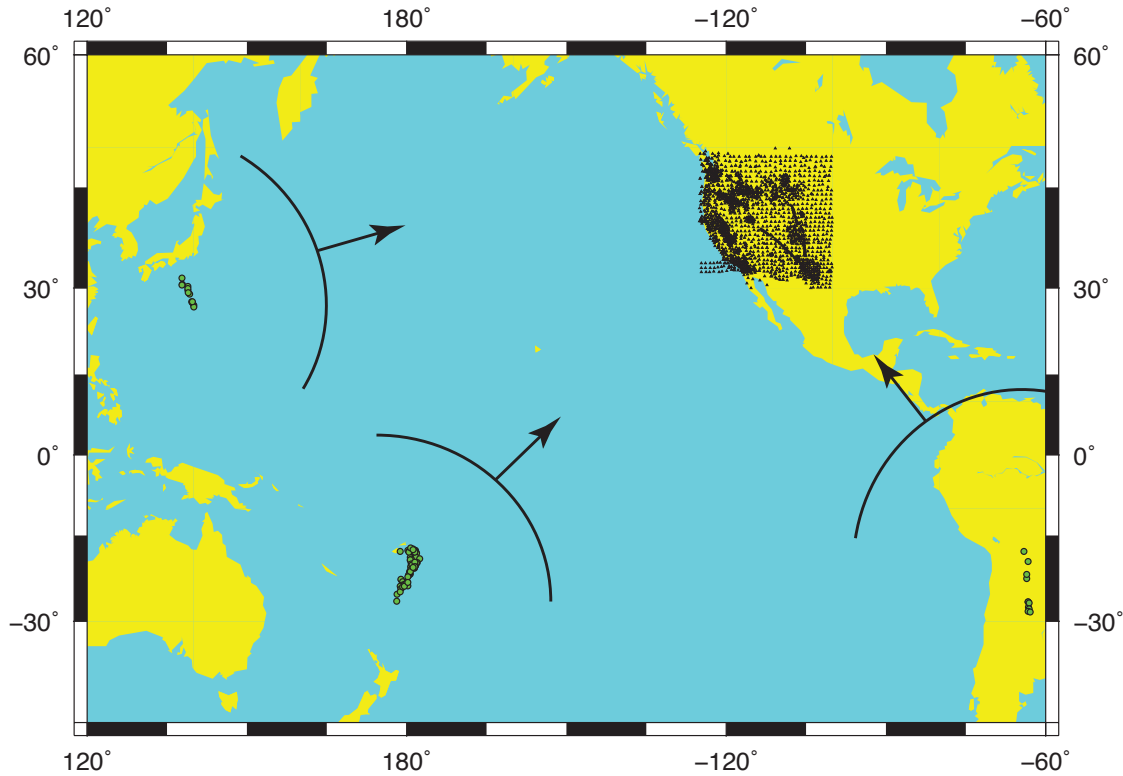
159 can, in principle, be sensitive to the effects of scatterers whose size may be on the order of or less
160 than the spacing of array elements.

161

162 These integrals can be discretized and set-up as a linearized inverse problem in which the
163 squared difference of the observed coherences and predicted coherences of an unknown power
164 spectrum are minimized. The discretized forms of eqs.2a-c and the object function to be
165 minimized are given in Appendix B of Cormier et al. (2020).

166

167 The coherence data we chose to invert were 3 groups of deep focus earthquakes (Marianas,
168 Tonga-Kermadec, and South America) observed by elements of the US array, transportable
169 array, and FLEX arrays deployed in the western US (Fig. 3). Deep focus events were chosen to
170 avoid the effects of heterogeneity concentrated in the upper mantle near the source and to
171 eliminate the effects of near source reflections. P waveforms of 21,205 deep focus earthquakes
172 having moment magnitudes M_w 5.8-6.2 were downloaded from the Data Management Center of
173 IRIS. About 40% of these had sufficiently high signal to noise ratios and simple apparent
174 source-time functions to include in the coherence measurements. Within each earthquake group,
175 measured coherences are averaged at all receiver pairs corresponding to a specific lag.
176 Wavefront healing due to propagation from the source to the teleseismic receivers and averaging
177 coherences at each lag over all earthquakes aid in eliminating any source-side heterogeneity
178 effects. A joint inversion of data comprising 3 wavefronts arriving from widely different
179 azimuths, whose rays cross at variable depths beneath the array, makes it possible to achieve a
180 sensitivity to heterogeneity scales on the order of the smallest spacing (10 km) of array elements.



181

182

183 **Figure 3.** Hypocenters (green dots) of three deep-focus earthquake groups and US and FLEX
 184 Array seismic stations (black triangles) used in the inversion of P wave coherence for the upper
 185 mantle heterogeneity spectrum.

186

187 The inclusion of the effects of the specific earthquake source-time functions and radiation
 188 patterns in u_{ref} are essential to isolating the effects of forward scattering from those of the source.

189 To achieve this for each event the reference synthetic seismogram u_{ref} at each array element was
 190 computed from the IRIS Syngine service (Nissen-Meyer, et al., 2014;

191 <https://service.iris.edu/irisws/syngine>) in the AK135-F Earth model (Montagner & Kennett,

192 1995) using the known moment tensor solution for each event from the GCMT service (Ekstrom
 193 et al., 2012; <https://www.globalcmt.org>) and an empirical source time function determined by

194 stacking P waves from each event in the 40° to 90° distance range. In conjunction with this paper
 195 we also provide a link to Python and Matlab scripts to assist researchers in designing

196 experiments with stochastic tomography (Tian and Cormier, 2020). These example scripts treat

197 the effects of earthquake moment tensors and source-time functions on the reference wavefields
198 defining coherence measurements.

199

200 2.2 Single layer inversion

201 As a first step it is useful to factor out the wavenumber dependence from a depth dependent
202 spectrum and compare its spectrum against published, non-depth dependent, stochastic models of
203 upper mantle heterogeneity. For understanding how lateral temperature differences drive mantle
204 heterogeneity such a comparison can also provide some constraints on the compositional and
205 temperature variations in the upper mantle. The coherence of broadband (0.02 to 2 Hz) body
206 waves can provide information at scale lengths intermediate between those estimated from global
207 travel-time tomography and the coda of higher-frequency body waves.

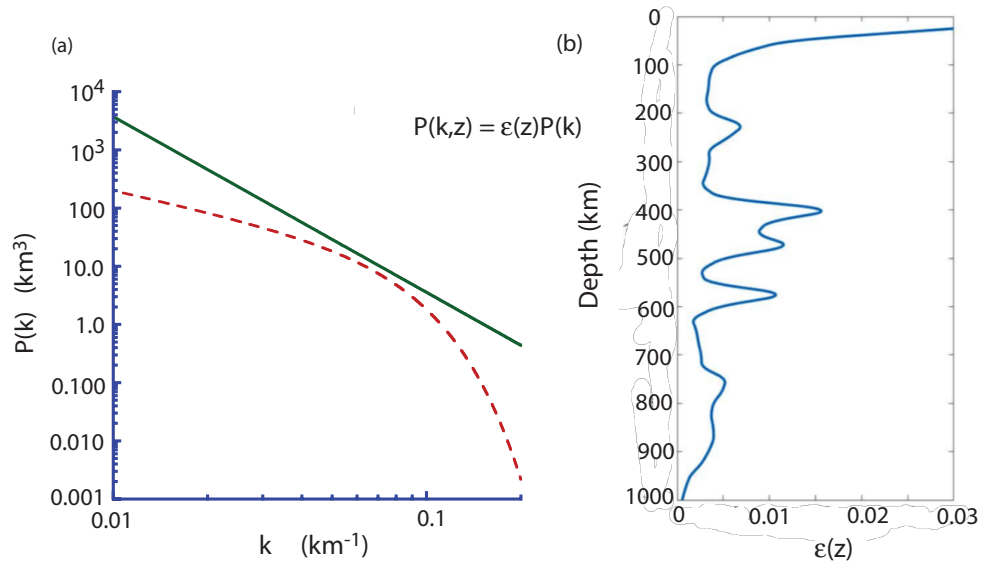
208

209 We thus first inverted for a uniform heterogeneity spectrum with depth in which the shape of the
210 power spectrum was defined by 4 parameters described in Cormier et al. (2020). To recognize
211 that the sensitivity of our coherence data peaked around a narrow band in wavenumber, we
212 employed a parameterization of the heterogeneity spectrum that consisted of a product of a low
213 pass and high pass filter in wavenumber (Klimes, 2002). Fig. 4a compares our inverted spectrum
214 for the upper 1000 km of the mantle to an overlapping band estimated by Mancinelli et al. (2016)
215 from scattered, low-frequency (<0.2 Hz), coda of teleseismic body waves. The two spectra
216 nearly coincide in a narrow wavenumber band centered near 0.065 km^{-1} . The dominant
217 frequency (0.7 Hz) of our P wave data in this wavenumber corresponds to a 100 km wavelength
218 in the upper mantle. At this center frequency, scattering will primarily be the Mie type in the
219 forward direction, with sensitivity strongest to heterogeneities having a scale between 10 to 100
220 km. A minimum detection threshold of 10 km scale agrees with the highest resolution
221 achievable by stochastic tomography with our smallest sensor spacings. It also agrees with our
222 detections and non-detections of phase changes predicted from thermodynamic modeling
223 (section 3).

224

225

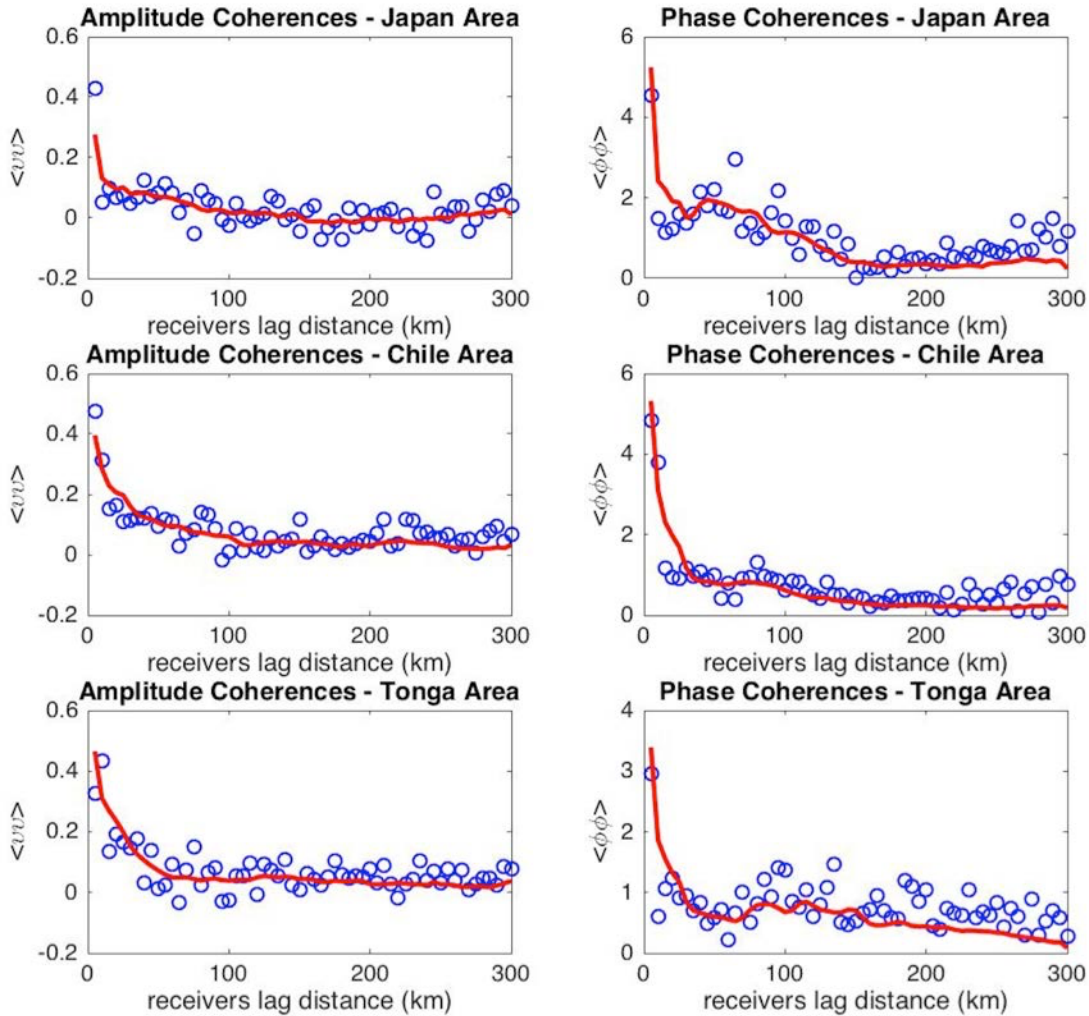
226



227

228 **Figure 4.** (a) Left: uniform power spectrum density of P velocity fluctuation for the upper 1000
 229 km of Earth's mantle determined from stochastic tomography (dashed red line) compared to an
 230 overlapping portion of Mancinelli et al.'s (2016) estimates for this depth range in the frequency
 231 band of teleseismic body waves, (solid green line), in which Mancinelli et al.'s 1-D spectrum
 232 has been converted to a 3-D isotropic spectrum for a von Kármán medium using formulas in Sato
 233 et al. (2012). (b) Left: smoothed depth-dependent model of this spectrum determined from
 234 stochastic tomography applied to the mantle beneath the western US (Cormier et al., 2020).

235



236

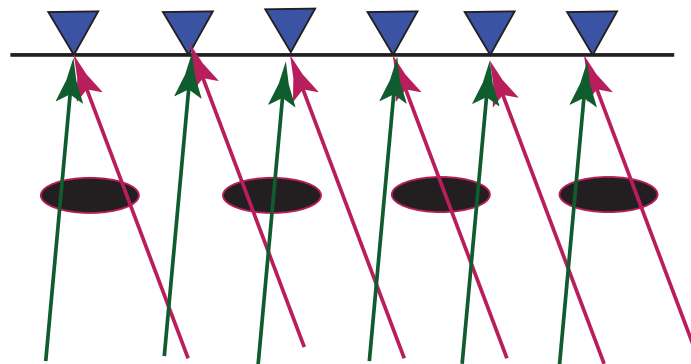
237 **Figure 5.** Observed coherences at all possible pairs of stations at specific lag distances (open
 238 circles) and predicted P wave coherence (solid lines) for a depth dependent model of mantle
 239 heterogeneity power (Fig. 4b) for the 3 epicentral regions shown in Fig. 3.

240 2.3 Depth dependent inversion

241 We next assumed that the spectral shape determined from the single layer inversion (Fig. 4a) was
 242 constant in depth but allowed its peak power to vary with depth in 40, 25 km thick, layers. Fig.
 243 4b plots the inverted depth dependence of P velocity fluctuation. Fig. 5 compares the predicted
 244 coherences for the depth dependent model with the observed coherences for the 3 epicentral
 245 regions. Compared to the uniform model, the squared coefficient of determination of
 246 coherences for the depth dependent model increased from 0.74 to 0.80. The reduced χ^2

247 computed from observed and predicted coherences decreased from 1.65 to 1.05. The
 248 significantly smaller, but not less than 1, χ^2 for the depth dependent spectrum is consistent with
 249 an improved fit, but not an over-fit due to the assumption of a larger number of unknown
 250 parameters. Interpretations of the depth dependent of model heterogeneity power are given in
 251 section 4.

252 The 25 km thick depth intervals, which are close to the smallest sensor spacings (10 to 20 km) of
 253 the denser FLEX arrays shown in Fig. 3, agree with the resolvable spatial scale determined in
 254 sensitivity tests conducted by Wu and Xie (1991). In that study, Wu and Xie applied a stochastic
 255 tomographic inversion to numerically synthesized seismograms in media having known depth-
 256 dependent heterogeneity spectra in the presence of noise. For coherence inversions that
 257 combined wavefronts arriving from different angles (e.g., Fig. 6), they found it possible to
 258 achieve a depth resolution equal to the spacing of sensor elements.



259
 260 **Figure 6.** Illustration of how incorporation of wavefronts arriving from different directions (red
 261 and green arrows) can enhance the resolution of small-scale heterogeneity (black ellipses).

262 3. Hefesto: a thermodynamic model of mantle composition and phase

263 3.1 Temperature derivatives of seismic velocity

264 Hefesto is a Fortran code for computing seismic velocities, densities, and other physical
 265 properties for silicate minerals that minimize the Gibbs free energy at specific temperatures and
 266 pressures (Stixrude and Lithgow-Bertelloni, 2005, 2007, 2022). Its input consists of pressure,
 267 temperature, and a bulk composition in the $\text{SiO}_2\text{-MgO-FeO-Al}_2\text{O}_3\text{-CaO-Na}_2\text{O}$ system, and

268 models of the properties of 51 end-members of 22 phases and their interactions. Among its
269 output options are elastic velocities and density, as a function of depth. Isomorphic (constant
270 phase) temperature derivatives of elastic velocity are calculated analytically but the additional
271 contribution of a metamorphic component in the midst of a solid phase change can be calculated
272 from difference derivatives determined by running the code at two closely spaced temperatures
273 (e.g., Fig. 1a and Stixrude and Lithgow-Bertelloni, 2007). In the results shown in this paper, we
274 calculated difference derivatives of, $d\ln V_p/dT$ to double precision on a 64 bit processor,
275 assuming either adiabatic or isothermal conditions, assuming two temperatures separated by 10°
276 K.

277 3.2 The metamorphic temperature derivative as a proxy for heterogeneity

278 Because the slope of the boundary between two stable silicate phases in P-T space is neither zero
279 or infinite, any lateral change in temperature will also be associated with a change in the pressure
280 (depth) of the phase boundary. This makes it possible for the temperature derivative of a to be
281 used as a proxy for locating and measuring the width of a zone in which the two phases are
282 competing for equilibrium (e.g. Fig. 2). Stixrude and Lithgow-Bertelloni (2007) have termed the
283 temperature derivative of velocity in this situation the metamorphic derivative in recognition that
284 its shape is affected by more than one form or phase of a mineral. The existence of two phases in
285 the zone of the phase transition, with differing seismic velocities and density can scatter body
286 waves. Hence, peaks in the predicted metamorphic component of the temperature derivative of a
287 seismic velocity will be associated with peaks in the heterogeneity spectrum as a function of
288 depth.

289 Implemented as a proxy for seismic velocity fluctuations, the values of $d\ln V_p/dT$ require a
290 conversion factor related to the mean lateral temperature variation to convert $d\ln V_p/dT$
291 predictions to estimates of the mean fluctuations of P velocity, dV_p/V_p . Stixrude and Lithgow-
292 Bertelloini (2012) find that an upper bound of 150° K for lateral temperature variations yield
293 lateral velocity variations in agreement with seismic tomography in the upper mantle. Solomon
294 (1976) also argues for 150° K lateral temperature variations from geodynamic considerations.
295 We apply a slightly more conservative estimate of 100° K from comparing the scale of P velocity
296 variations (order of 1 %) inferred from P travel time tomography to thermodynamic estimates of

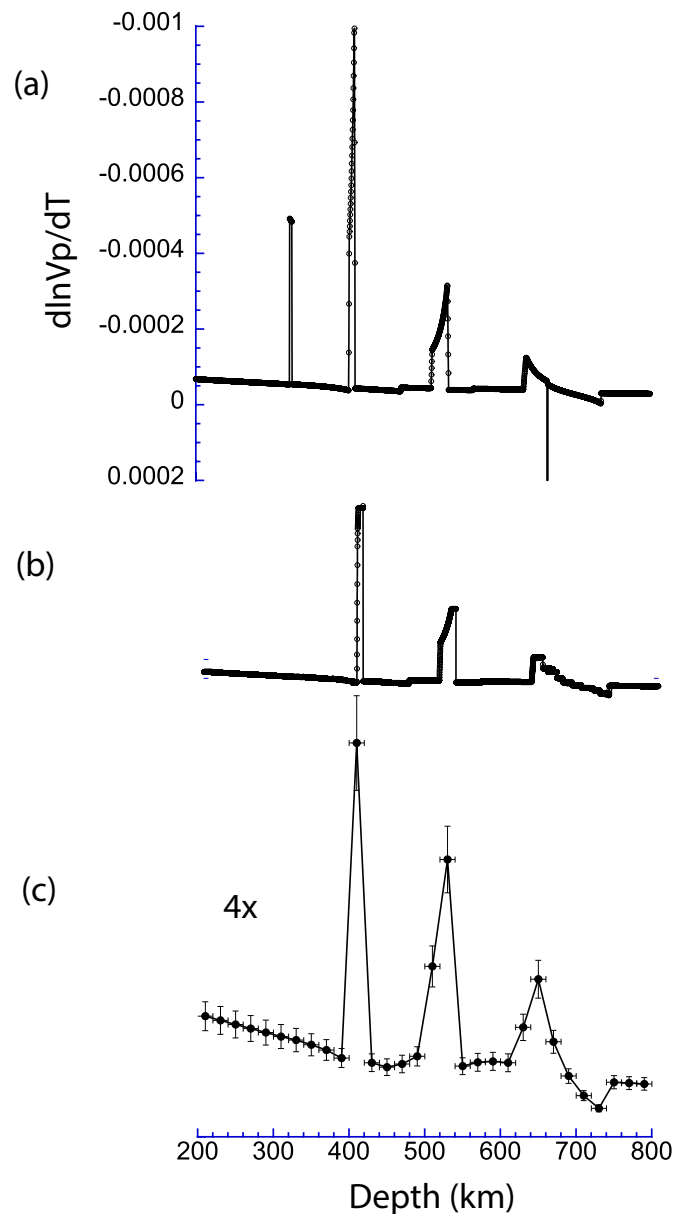
297 the isomorphic temperature derivative (the temperature derivative not in a region of a phase
298 change). An alternative estimate of this conversion factor, not related to any assumption of
299 lateral temperature differences, is to estimate the maximum velocity fluctuation in a phase
300 transition zone between two competing phases. This is simply the difference in velocities
301 between two depth sides of a phase change divided by the average of the two velocities. For the
302 410 km phase change, this value is 3% from the Hefesto estimated velocity changes for both
303 pyrolite and harzburgite/basalt mixtures. This leads to the identical conversion factor of 150° K
304 at 410 km. Given the existence of uncertainties in the lateral temperature differences and the
305 precise shape of the heterogeneity spectrum and its variation across the zone of a phase change,
306 we estimate that the true magnitude of P velocity fluctuations within most of the phase changes
307 occurring over zones wider than a wavelength is likely to lie between 1 to 3%.

308

309 3.3 Filtering for sensitivity compatible with stochastic tomography

310 A phase change that occurs over a depth range less than 6 km wide is unlikely to be detected as
311 narrow zone of increased heterogeneity that can be resolved by stochastic tomography applied to
312 sensor spacings between 10-20 km and coherence averaged over lag intervals 25 km and greater.
313 The 660 km phase change from ringwoodite to ferropericlase and magnesiowustite is estimated to
314 be 1-2 km wide in agreement with both other computational and experimental estimates in
315 mineral physics. Another phase change near 300 km depth from ortho-pyroxine to high pressure
316 clinopyroxene (opx to hcp_x) is also quite narrow, Hefesto predicting it to occur over 8 km. Such
317 phase changes occurring over depth zones less than 10 km width are easily detected from
318 reflected and converted body waves. This is especially the case for 660 km phase change, which
319 has been observed in reflections at 1-2 Hz. The non-detection of the 660 km and 300 km phase
320 changes in our stochastic tomography inversions, sensitive to phase changes wider than 6 km, is
321 consistent with their narrowness. To compare Hefesto predictions with our stochastic
322 tomography inversions, we have hence applied a median filter to remove phase transitions less
323 than a body wavelength wide, and an averaging window nearly equal to observed coherence lag
324 intervals, to each point shown in comparison plots. This median filter, often used to remove
325 electronic spikes in seismic recordings (Evans, 1982), was designed to remove all signals in the

326 metamorphic derivatives that are less than 6 km wide. Fig. 7 shows an example in which the
327 median filter and averaging window has been applied to the Hefesto predicted temperature
328 derivatives of P velocity.



329

330 **Figure 7.** (a) Hefesto $d \ln V_p / dT$ computed for a pyrolite model of the upper mantle; (b) followed
331 by median filtering applied to (a) to remove signals less than 6 km wide; and (c) followed by 20
332 km wide depth averaging applied to (b).

333

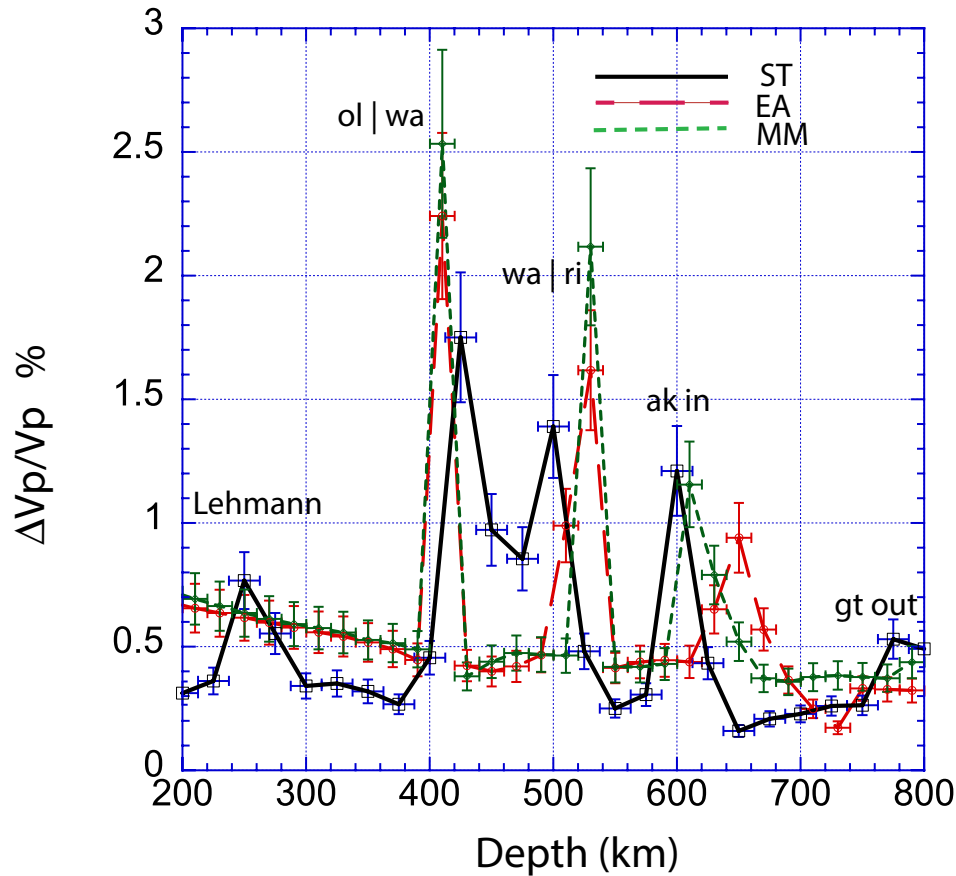
334

335 **4 Results**

336 4.1 Interpretation of the depth dependent heterogeneity spectrum

337 Results of our inversion for a depth dependent heterogeneity spectrum for the upper 1000 km of
338 the mantle beneath the western US for the root-mean-square (rms) P velocity fluctuations are
339 shown in Fig. 8. These are compared with the Hefesto predictions for P velocity fluctuations
340 derived from the temperature derivatives of P velocity. The Hefesto predictions, for both an
341 equilibrium pyrolite composition (EA) and a mechanical mixture of harzburgite and basalt
342 (MM), are filtered and averaged to agree with the estimated sensitivities of stochastic
343 tomography (section 3). For the P velocity fluctuation predicted from stochastic tomography, the
344 horizontal uncertainty bars in depth in Fig. 8 are fixed at 25 km in length to represent the spacing
345 between averaged coherence lags, while maintaining a reduced chi-square greater than 1
346 calculated from predicted and observed coherences. For the P velocity fluctuations estimated
347 from Hefesto, the horizontal uncertainty bars are the width of a 20 km moving depth average of
348 the filtered temperature derivative of velocity. From numerical experiments recording the change
349 in the peak value of the predicted velocity fluctuation as the starting depth of the moving average
350 changes, the ordinate uncertainty bars are taken to be $\pm 10\%$ of the median peak value.

351



352

353 **Figure 8.** Solid black line (ST): the depth dependent heterogeneity spectrum for the rms
 354 fluctuation of P wave velocity in the upper 1000 km of the mantle estimated from stochastic
 355 tomography. Long dashed red line (EA): filtered temperature derivative of P velocity predicted
 356 for an equilibrium pyrolite model. Short dashed green line (MM): filtered temperature derivative
 357 of P velocity predicted for a mechanical mixture of 80% harzburgite and 20% basalt. Each
 358 thermodynamic prediction assumes an adiabatic temperature profile having a 1600° K. potential
 359 temperature. Interpreted detections of the Lehmann discontinuity and upper mantle mineral
 360 phase changes are labeled above or near peaks.

361

362

363 The Hefesto predicted peaks in the temperature derivative of seismic velocities are from
 364 metamorphic contributions due to changes in constituent mineral phases required to minimize
 365 Gibbs free energy. Runs are shown for an equilibrium pyrolite model and a mechanical mixture
 366 of harzburgite and basalt to simulate the effects of slab cycling. The expression of phase changes

367 can either be sharp or spread out over a depth range bounded by two changes in the gradient of
368 seismic velocity. If sharp (less than 10 km in width), the phase change can be easily detectable
369 from reflected, converted, or multi-pathed body waves. In these cases the effect of lateral
370 temperature variations will be expressed as topography on an apparent seismic reflector rather
371 than a zone of increased heterogeneity. The predicted phase change at 660 km of ringwoodite to
372 Mg-perovskite and magnesiowusite is one such example. Phase changes wider than 10 km in
373 depth may not be detectable in seismic reflections or receiver functions, but will be detectable
374 from stochastic tomography as a zone of discrete scatterers in a narrow range of depth close to
375 the width of a peak in the filtered Hefesto prediction for the temperature derivative of P velocity.
376 For these phase changes, the horizontal length scale of the scatterers will be related to the lateral
377 scale of temperature variations and the vertical scale to the width of the depth (pressure) range
378 over which the phase change occurs.

379

380 4.2 Largest peaks in the depth dependent heterogeneity spectrum

381 The depths and relative amplitudes of at least three of the peaks in the heterogeneity spectrum
382 measured by stochastic tomography agree well enough with those predicted by Hefesto to have
383 confidence in an identification of the detected phase change. These are:

384

- 385 (1) a peak at 425 ± 12 km depth nearly matches a Hefesto predicted phase change of olivine
386 to wadsleyite (ol | wa) at 412 km occurring over a 10 km width;
- 387 (2) a peak at 500 ± 12 km depth matches a Hefesto predicted phase change of wadsleyite to
388 ringwoodite (wa | ri) at 500 km occurring over 20 km width;
- 389 (3) in mechanical mixtures of harzburgite and basalt (MM), a peak at 600 ± 12 km matches
390 the interference of two predicted phase changes, each exothermic with positive
391 temperature derivatives of velocity. Together they occur over a 30 km width. In
392 equilibrium pyrolite, these phase changes are predicted to be deeper at 640 km depth.

393

394 At 600 km depth the predicted signal in the temperature derivative of velocity consists of a
395 relatively wide peak in which the shallower wadsleyite to ringwoodite phase change
396 interferes with an initiation of a deeper calcium perovskite phase (capv in). The 600 km
397 initiation of akimotoite is not the deeper endothermic phase change associated with the

398 sharp discontinuity commonly detected near 660 km. For some compositions and
399 temperatures, Hefesto predicts the 660 km phase change to occur over two sharp, and
400 closely spaced depths. These two deeper phase changes are too sharp to be detected by
401 stochastic tomographic with the array and frequency band of this study. Both seismic
402 observations and mineral physics studies (e.g., Ishii et al., 2001), predict a 660 km deep
403 phase change to occur over a zone equal to or less than 2 km. In the median filtered Hefesto
404 predictions shown in Figs. 7c and 8 the phase changes near 660 km vanish, but appear in
405 the unfiltered Hefesto prediction shown in Fig 7a.

406

407 If our estimated error bars in depth are close to truth, the 600 km phase change detected
408 from stochastic tomography favors a harzburgite rather than a pyrolite composition in the
409 mantle transition zone. Within error bars, our stochastic tomography detection at 500 km
410 depth for the wadsleyite to ringwoodite phase change is shallower than either the Hefesto
411 predictions for either pyrolite or a mechanical mixture. The disagreement is similar for both
412 compositional models, suggesting that a better agreement may be achieved either by
413 revising the Hefesto inputs for the physical properties of individual minerals or by revising
414 the temperature profile. Of these two inputs, the depth of phase changes is most strongly
415 sensitive to the temperature profile. In section 5, we discuss how a negative temperature
416 perturbation in the 410 to 660 km transition zone, consistent with a history of subduction,
417 can bring the observed and predicted heterogeneity spectra into closer agreement.

418

419 4. 3 Smaller peaks in the depth dependent heterogeneity spectrum

420

4.3.1 775 km

421 Another peak requiring a small negative perturbation to an assumed adiabatic temperature
422 profile having a 1600 deg K potential temperature is a peak at 775 ± 12 km. This peak
423 nearly correlates with a Hefesto predicted phase change at 795 km in mechanical mixtures
424 of basalt and harzburgite having a basalt fraction of 18%, indicative of a phase change in
425 subducted oceanic crust. The Hefesto predicted phase change in the temperature derivative
426 consists of relatively weak peak having a 7 km width.

427

428

4.3.2 250 km

429 The heterogeneity peak at 250 km \pm 12 km is neither the orthopyroxene to high pressure
430 clinopyroxene phase change predicted closer to 300 km or the X discontinuity found in many
431 receiver function studies (Pugh, 2021), both of which are too narrow (<10 km) to be detected by
432 stochastic tomography and the filtered Hefesto predictions shown in Figs. 7bc and 8. We instead
433 interpret this to be a signal associated with the Lehmann discontinuity, which is frequently
434 detected in S body wave studies at depths 220 km to 240 km beneath continents (e.g., Vinnik et
435 al., 2015). Karato (1992) has suggested that the Lehmann discontinuity is associated with a
436 change in rheology from dislocation creep above to diffusion creep below a 20 km wide or
437 greater zone centered near 240 km depth for wet and/or hot conditions. This transition is also
438 associated with a change from an anisotropic lithospheric lid to an isotropic asthenosphere. A
439 change in anisotropy and rheology, however, is unlikely to be strongly expressed by a zone of
440 heterogeneity capable of scattering seismic waves. Vinnik et al. (2005) have also shown that a
441 change in rheology and anisotropy alone cannot account for the sign of the S to P conversion of
442 S waves incident on the Lehmann discontinuity. A possible mechanism for heterogeneity in this
443 depth region may be the hypothesis of Ono (2007), who proposes that the Lehmann is due to the
444 effects of dehydration of subducted oceanic sediments beneath a continent. A possible
445 supporting piece of evidence for this hypothesis is that Hefesto does not yet include the effects of
446 H₂O content on melting and dehydration.

447

448 4.4 Modeling considerations: resolution and temperature profile

449 The differences between detected and predicted phase changes will depend on the accuracy of
450 the assumptions in the thermodynamic model and the sampling and errors in the power spectrum
451 of heterogeneity determined from stochastic tomography. The depth accuracy of the
452 thermodynamic model depends on the validity of the assumed petrologic model, the physical
453 properties of minerals determined from combinations of experimental observations and ab initio
454 calculations, and the assumed temperature profile. The accuracy of the power spectrum estimated
455 from stochastic tomography largely depends on the depth-sampling rate that can be resolved in
456 the inversion of coherences, which depends on sensor spacing and its geometry and the
457 azimuthal and depth distribution of seismic events.

458

459 The disagreement between the detected (600 km) and predicted (660 km), last and deepest,
460 endothermic phase change is too large to be explained by a plausible hotter mantle temperature
461 in this broad region. A global 660 km discontinuity has been largely confirmed in many seismic
462 studies and is generally the most robustly detected discontinuity even by reflected body waves
463 having dominant frequencies approaching 1 Hz (e.g., Deuss et al., 2006). Its signature in
464 receiver functions (Andrews & Deuss, 2008), however, can be complex, in agreement with the
465 complex phase changes predicted from thermodynamic models at and near this depth (Xu et al.,
466 2008). A partial explanation for a positive detection at 600 km but not 660 km is that the 25 km
467 sampling rate in the inversion is simply too coarse to resolve the complex signal of two closely
468 spaced phase changes. We thus conclude that our detection at 600 km is the transformation of
469 high-pressure clinopyroxene to akimotoite initiating closer to 600 km than 650 km. Hao et al.
470 (2019) predict this transition to have a width on the order of 25 km or greater. The detection of
471 an akimotoite transition at 600 km, indicative of the existence of regions of colder mantle
472 temperatures (Hogrefe et al., 1994), coupled with a phase transition in basalt at 775 km, is
473 consistent with the history of the subduction of the Farallon plate beneath the western US.
474 Tomographic images of the shear velocity structure of the mantle beneath this region reveal
475 evidence of both slab stagnation and fragmentation in the lower mantle transition zone as well as
476 penetration beneath 660 km (Schmid et al., 2002).

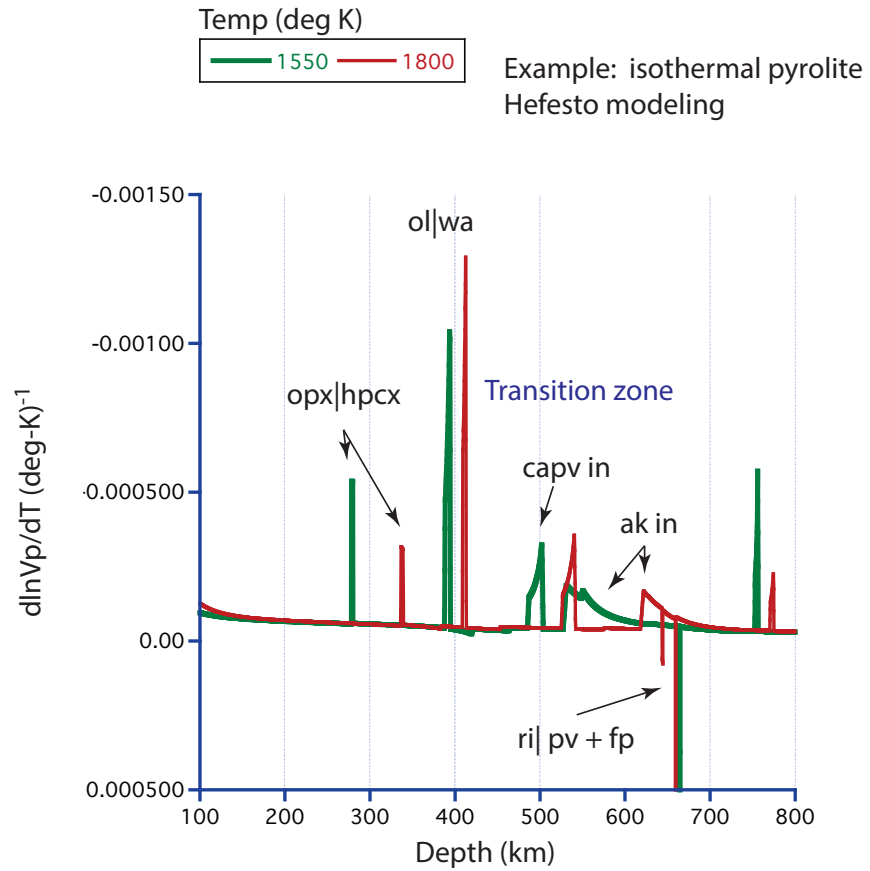
477

478

479 4.5 Geotherm perturbation

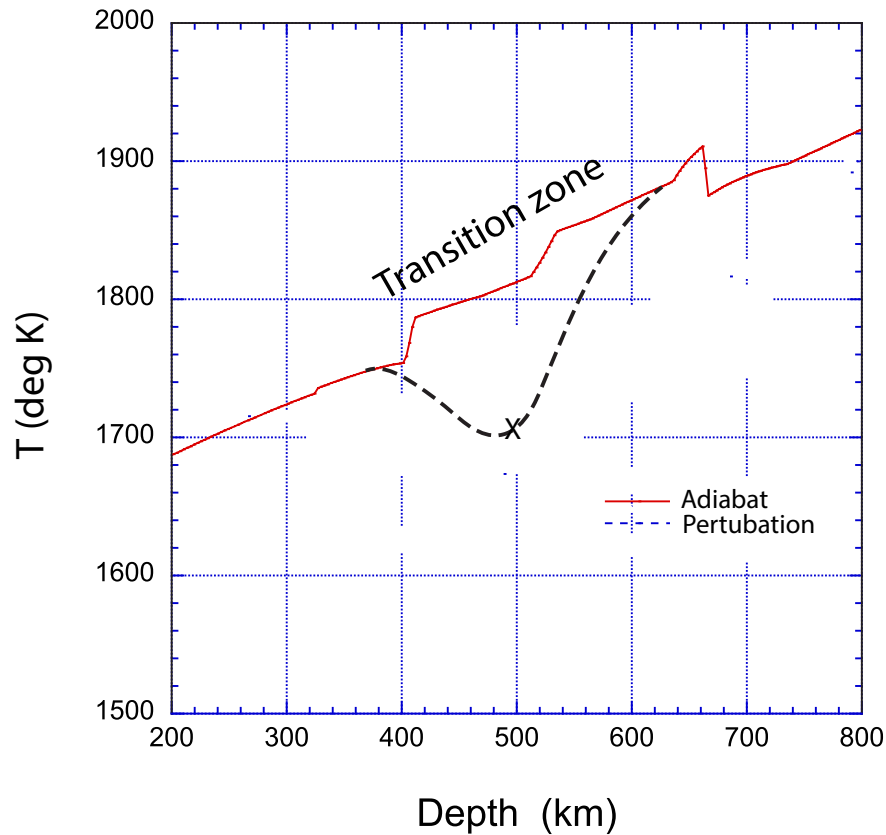
480 Two isothermal runs of Hefesto (Fig. 9) demonstrate the relative sensitivity of different predicted
481 phase transition to changes in temperature. The 410 and 660 km phase transitions are
482 considerably less sensitive to lateral temperature variations than the calcium perovskite and
483 akimotoite transitions near 500 and 600 km depth, respectively. Hence, if the physical properties
484 and chemistry of these two transitions are well understood, they can potentially serve as accurate
485 thermometers in the transition zone. Assuming that errors in of the chemistry and physical
486 properties taken as inputs to Hefesto are small, we can estimate the temperature required to make

487 the transition zone phase changes come into better agreement with our measurements of
488 heterogeneity in the transition zone from stochastic tomography. The perturbation needed to
489 achieve this (Fig. 10) requires a cooler transition zone temperature compared to that calculated
490 for a mantle adiabat having a 1600° K potential temperature. It is also worth noting that the
491 negative temperature perturbation required to bring the akimotoite phase transition at 600 km
492 into better agreement with a pyrolite model may not require as high a percentage of harzburgite
493 in models having a mechanical mixture (Zhao, et al., 2022). An example applying this
494 temperature perturbation is shown in Fig. 11. The size and form of this perturbation is similar to
495 those proposed in mantle convection studies by Tackley (1993) and Matyska and Yuen (2002),
496 who predict non-adiabatic perturbations to the mantle geotherm due to slab stagnation in the
497 transition zone. In addition to the results shown here from stochastic tomography, travel time
498 tomography also supports this condition for the subduction of the Farallon slab beneath the
499 western US. East-west cross sections of the P wave tomographic model LLN3D are consistent
500 with a fast, cool, region in the mantle transition zone (Fig. 12).



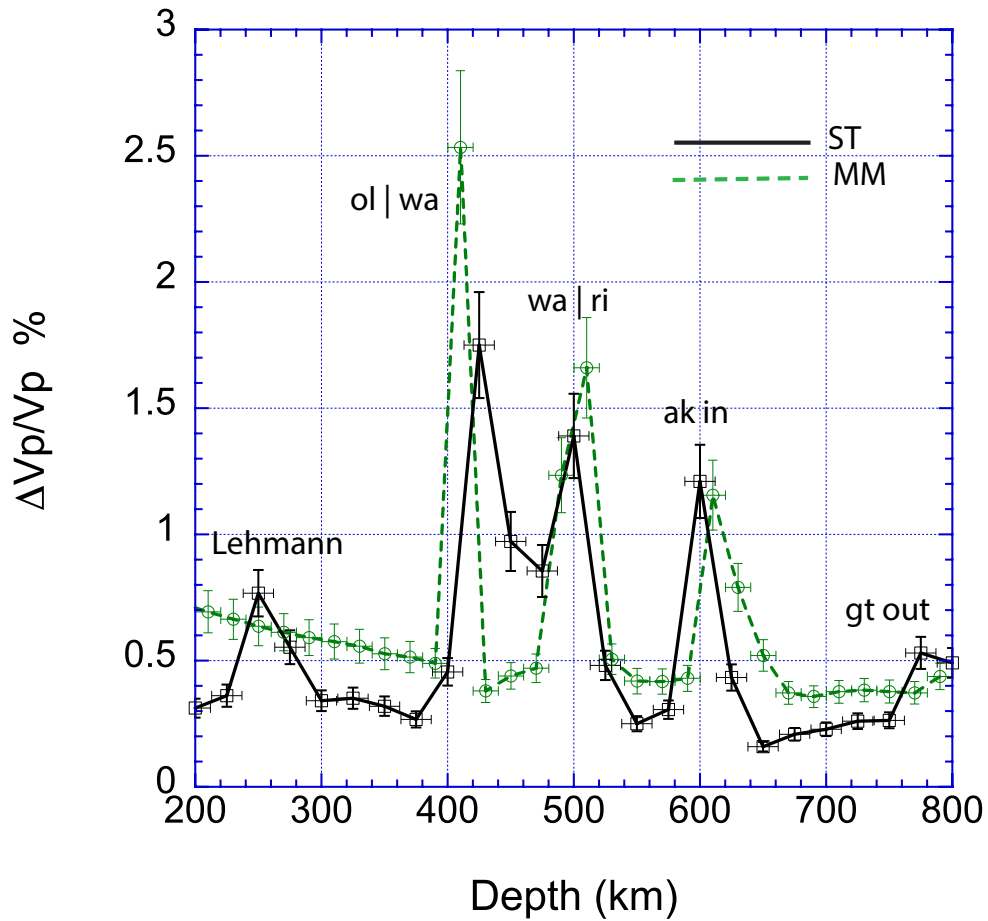
501

502 **Figure 9.** Isothermal calculations of $d\ln V_p/dT$ for pyrolite for 1600° K. and 1800° K.



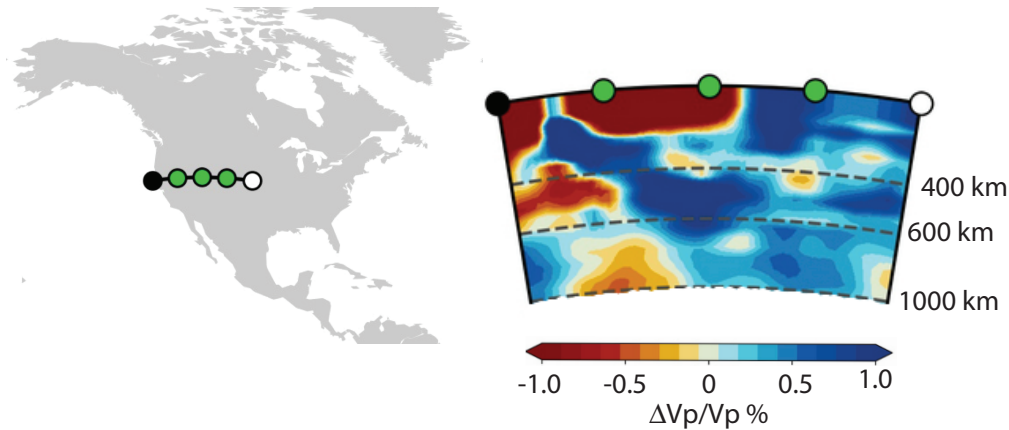
503

504 **Figure 10.** A perturbation (dashed) is applied in an adiabatic temperature profile in the
505 transition zone to achieve better agreement between the peaks in heterogeneity determined from
506 stochastic tomography and those predicted by the Hefesto thermodynamic code. The X marks the
507 temperature perturbation needed to make depth of the wadsleyite to ringwoodite phase transition
508 predicted from an isothermal run of Hefesto agree with the 500 km deep peak found from
509 stochastic tomography.



510

511 **Figure 11.** Solid black line (ST): mantle heterogeneity spectrum of P waves measured from
 512 stochastic tomography applied to the western US. Short green dashed line (MM): temperature
 513 derivative calculated from the Hefesto thermodynamic code for a mechanical mixture of
 514 harzburgite and basalt assuming the temperature perturbation in the transition zone shown in
 515 Figure 10.



516

517 **Figure 12.** Cross-section of P velocity structure beneath the western US along an E-W profile
 518 centered at 50 deg latitude from the LLN3D model of Simmons et al. (2012, constructed from
 519 SubMachine web tools (Hosseini et al., 2018).

520 The combination of mechanisms creating slab stagnation are still actively debated, depending on
 521 slab rollback at the initial subduction zone, the fine structure of the endothermic phase change
 522 near 660 km, its Clapeyron slope, and whether there is a viscosity increase or decrease below the
 523 660 km phase change (e.g., Mao and Zhong, 2008). The non-detection of 660 km phase change
 524 from stochastic tomography, its otherwise ubiquitous detection from reflected and converted
 525 high frequency (> 1 Hz) body waves (e.g., Whitcomb and Anderson, 1970), the narrow width of
 526 metamorphic temperature derivatives of its P and S wave velocity changes, and its topography
 527 are all consistent with it being an endothermic phase change, very narrow in width (no more than
 528 2-10 km), with a near vertical Clapeyron slope.

529

530

531

532 **5 Conclusions**

533 From stochastic seismic tomography applied to the upper 1000 km of the western US, we have
534 shown that its heterogeneity spectrum is characterized by a series of peaks related to narrow
535 regions of depth in which phase or chemistry changes. We have demonstrated the stochastic
536 seismic tomography can capture higher order phase and chemical changes in the upper mantle
537 that are undetectable from reflection imaging. These peaks, having amplitudes on the order of 1-
538 2% in P velocity fluctuation, strongly correlate with the majority of predicted phase changes
539 from thermodynamic models of the upper mantle's chemistry and phase. Stochastic tomography
540 has the potential to detect mantle phase changes that do not exhibit changes in seismic velocity
541 and density over short depth intervals. These types of phase changes are characterized by paired
542 changes in velocity gradient over a transition depth that may be equal to or larger than the
543 wavelength of a body wave. Results from a depth-sampling interval of 25 km for the inverted
544 spectrum suggest that many of these phase changes may occur over a range in depth equal to or
545 greater than 25 km. An exception is our non-detection of the phase transition at 660 km,
546 consistent with a transition interval in depth that may be as small as 2 km (0.1 GPa).

547

548 Our interpretation of individual peaks in the heterogeneity spectrum as a function of depth are
549 consistent with a history of subduction and slab stagnation in the upper mantle transition zone
550 between 400 to 660 km depth. This interpretation is based largely on the depth position and
551 temperature dependence of the detected wadsleyite to ringwoodite transition at 500 km depth and
552 the calcium perovskite to ringwoodite transition at 600 km depth. A stochastic tomography
553 detection of a smaller phase transition near 250 km is interpreted to be the Lehmann
554 discontinuity, which is unpredicted by thermodynamic modeling not containing effects of water,
555 and which may be the signature of dehydration of subducted oceanic sediments. The depths of
556 the 500 km, 600 km, and a 775 km phase change require a negative perturbation of a mantle
557 adiabat in the transition zone, extending at least 100 km below the 660 km phase transition. This
558 cool perturbation is consistent with the predictions of mantle convection suggesting slab
559 stagnation in the transition zone, with the predictions of thermodynamic modeling incorporating

560 perturbations to the geotherm, and with fast P velocities in the mantle transition zone found in 3-
561 D travel time tomography of the western US.

562

563 To detect the thermodynamically predicted changes in mantle silicates with stochastic
564 tomography, we demonstrate that a depth sampling interval of 25 km or less must be achieved.
565 Such a resolution may generally also require an estimation of the amplitude and phase effects of
566 source radiation patterns and source-time functions. Averaging of coherence lags over all pairs of
567 sensors having a common lag distance over a large number of earthquakes arriving from
568 different azimuths will enable heterogeneities having scale lengths on the order of the sensor
569 spacing to be detected and will also tend minimize site effects at the near surface of sensors. The
570 10-20 km spacing of a growing number of FLEX array experiments of the US Array and the
571 availability of waveforms from 3 widely separated groups of deep focus earthquakes, having
572 simple source-time functions, makes this high resolution possible for at least the western US.
573 Our location of phase changes represents an average for the western US for depths between 200
574 km and 1000 km, between latitudes 30° N and 50° N and longitudes 100° W and 125° W.
575 Quantification of lateral variations in these phase changes over smaller regions of the upper
576 mantle will depend on the densities and duration of FLEX array experiments and the availability
577 of body wavefronts arriving from different azimuths.

578 **Acknowledgments and Data**

579 This study incorporated work initially funded by the National Science Foundation under grant
580 EAR 14-46509 (Vernon Cormier) and grant EAR 16-21878 (Yingcai Zheng). Figure 3 was
581 drawn using the Generic Mapping Tools (Wessel and Smith, 1998).

582

583 Waveform data and services for centroid moment tensors and synthetic seismograms are
584 available from the Incorporated Research Institutions for Seismology through the web site
585 <https://www.iris.edu>. Matlab and Python scripts for processing and inverting amplitude and
586 phase coherences for single layer and depth dependent heterogeneity spectra are available from
587 the web site listed in the Tian & Cormier (2020) entry References. The Hefesto thermodynamic
588 mineral code is available at the web link: <https://github.com/stixrude/HeFESToRepository>.

589

590 **References**

591 Andrews, J., & Deuss, A. (2008), Detailed nature of the 660 km region of the mantle from global
592 receiver function data. *J. Geophys. Res.*, 113 (B6). doi:10.1029/2007JB005111.

593

594 Blundell, S.J., & Blundell, K.M. (2014), Ch. 28 In: *Thermal Physics*, Oxford University Press,
595 Oxford, UK.

596

597 Burdick, L.J., & Helmberger, D.V. (1978), The upper mantle P velocity structure of the western
598 United States. *J. Geophys. Res.*, 83 (B4), 1699-1712.

599

600 Chu, R., Schmandt, B., & Helmberger, D.V. (2012), Upper mantle P velocity structure beneath
601 the midwestern US derived from triplicated waveforms, *Geochem. Geophys., Geosys.*, 13 (2), doi:
602 10.1029/2011GC003818.

603

604 Cormier, V.F., Tian, Y., & Zheng, Y. (2020), Heterogeneity spectrum of Earth's upper mantle
605 obtained from the coherence of teleseismic P waves. *Commun. Comp. Phys.*, 28, 74-97. doi:
606 10.4208/cicp.OA-2018-0079.

607

608 Deuss., A., Redfern, S.A.T., Chambers, K., & Woodhouse, J.H. (2006), The nature of the 660
609 km discontinuity in Earth's mantle from global seismic observations of PP precursors. *Science*,
610 311, 198-201.

611

612 Ekstrom, G., Nettles, M., & Dziewoski, A. M. (2012), The global CMT project 2004-2010:
613 Centroid moment tensors for 13,017 earthquakes. *Phys. Earth Planet. Int.*, 200-201, 1-9, doi:
614 10.1016/j.pepi.2012.04.002.

615

616 Evans, J.R. (1982), Running median filters and a general despiker, *Bull. Seism. Soc. Am.*, 72(1),
617 331-338.

618

- 619 Hao, S., Wang, W., Qian, W., & Wu, Z. (2019), Elasticity of akimotoite under the mantle
620 conditions: Implications for multiple discontinuities and seismic anisotropies at the depth ~600-
621 750 km in subduction zones. *Earth Planet. Sci. Lett.*, 528, 115830.
- 622
- 623 Hogrefe, A., Rubie, D.C., & Sharp, T.G. (1994), Metastability of enstatite in deep subducting
624 lithosphere. *Nature*, 372 351-353.
- 625
- 626 Hosseini, K., Matthews, K.J., Sigloch, K., Shepard, G.E., Domeier, M., & Tsekhmistrenko, M.
627 (2018), SubMachine: Web-based tools for exploring seismic tomography and other models of
628 Earth's deep interior, *Geochem., Geophys., and Geosys.*, 19(5), 1464-1483, doi:
629 10.1029/2018GC007431.
- 630
- 631 Karato, S. (1992), On the Lehmann discontinuity, *Geophys. Res. Lett.*, 19, 2255– 2258.
- 632
- 633 Ishii, T., Huang, T., Myhill, R., Fei, H. Koemets, L., Liu, Z., Maeda, F., Yuan, L., Wang, L.,
634 Druzhbin, D., Yamamoto, T., Bhat, S., Faria, R., Kawazoe, T., Tsujino, N., Kulik, E., Higo, Y,
635 Tange, Y., & Katsura, T. (2019), Sharp 660-km discontinuity controlled by extremely narrow
636 binary post-spinel transition. *Nature Geoscience*, 12, 869-872.
- 637
- 638 Klimes, K. (2002), Correlation functions of random media. *Pure Appl. Geophys.*, 159 1811-
639 1831.
- 640
- 641 Mao, W., & Zhong, S., (2008), Slab stagnation due to a reduced viscosity layer beneath the
642 mantle transition zone, *Nature Geosci.*, 11, 876-881.
- 643
- 644 Mancinelli, N., & Shearer, P., Liu, Q. (2016), Constraints on the heterogeneity spectrum of
645 Earth's upper mantle. *J. Geophys. Res.*, 121 (5), 3703-3721.
- 646
- 647 Matyska, C., & Yuen, D.A. (2002), Bullen's parameter eta: a link between seismology and
648 geodynamical modelling, *Earth. Planet. Sci. Lett.*, 198, 471-493.
- 649

- 650 Montagner, J.P., & Kennett, B.L.N. (1995), How to reconcile body-wave and normal-mode
651 reference Earth models? *Geophys. J. Int.*, 135-229-248.
- 652
- 653 Nissen-Meyer, T., van Driel, M., Stähler, S. C., Hosseini, K., Hempel, S., Auer, L., Colombi, A.,
654 & Fournier, A. (2014) AxiSEM: broadband 3-D seismic wavefields in axisymmetric media.
655 *Solid Earth*, 5, 425-445, <https://doi.org/10.5194/se-5-425-2014>.
- 656
- 657 Ono, S. (2007), The Lehmann discontinuity due to dehydration of subducted sediment, *The Open*
658 *Mineralogy Journal*, 1(1), 1-4, doi: 10.2174/1874456700801010001.
- 659
- 660 Pugh, S., Jenkins, J., Boyce, A., & Cottar, S. (2021) Global receiver function observations of the
661 X-discontinuity reveal recycled basalt beneath hotspots, *Earth Planet. Sci. Lett.*, 561, doi:
662 10.1016/j.epsl.2021.116813.
- 663
- 664 Sato, H., Fehler, M.C., & Maeda, T. (2012), *Seismic Wave Propagation and Scattering in the*
665 *Heterogeneous Earth*, 2nd edn., Springer-Verlag.
- 666
- 667 Schmid, C., Goes, S., van der Lee, S., & Giardini, D. (2002), Fate of the Cenozoic Farallon slab
668 from comparison of kinematic thermal modeling with tomographic images. *Earth and Planet.*
669 *Sci. Lett.*, 204, 17-32.
- 670
- 671 Shearer, P. (1991), Constraints on upper mantle discontinuities from observations of long-period
672 reflected and converted phases. *Journal of Geophysical Research*, 96(B11), 18,147– 18,182.
- 673
- 674 Simmons, N.A., S.C. Myers, G. Johannesson, & E. Matzel (2012), [LLNL-G3Dv3: Global P-](#)
675 [wave tomography model for improved regional and teleseismic travel time prediction](#), *J.*
676 *Geophys. Res.*, 117, doi:10.1029/2012JB009525.
- 677
- 678 Solomon, S.C. (1976), Geophysical constraints on radial and lateral temperature variations in the
679 upper mantle, *Am. Mineral.*, 61(7-8), 788-903.

680

681 Stixrude, L., & Lithgow-Bertelloni, C. (2007), Influence of phase transformations on lateral
682 dynamics in Earth's mantle. *Earth Planet. Sci. Lett.*, 263, 45-55.

683

684 Stixrude, L., & Lithgow-Bertelloni, C. (2012), Geophysics of chemical heterogeneity in the
685 mantle. *Ann. Rev. Earth Planet. Sci.*, 40, 569-595, doi:
686 10.1146/annurev.earth.36.031207.124244.

687

688 Stixrude, L., & Lithgow-Bertelloni, C. (2022), Thermal expansivity, heat capacity and bulk
689 modulus of the mantle, *Geophys. J. Int.*, 228(2), 1119-1149, doi: 10.1093/gji/ggab394.

690

691 Tackley P.J., Stevenson, D. J., & Glatzmaier G.A. (1993), Effects of an endothermic phase
692 transition at 670 km depth in a spherical model of convection in the Earth's
693 mantle. *Nature* 361:699-704

694

695 Tian, Y., & Cormier, V.F., (2020), https://github.com/vernoncormier/stochastic_tomography,
696 doi:10.528/zenodo.4000538.

697

698 Tkalčić, H., Cormier, V.F., Kennett, B.L.N., & He, K. (2010), Steep reflections from the Earth's
699 core reveal small-scale heterogeneity in the upper mantle. *Phys. Earth Planet. Int.*, 178, 80-91.
700 doi: 10.1016/j.pepi.2009.08.004.

701

702 Vinnik, L., Kurnik, E., & Farra, V. (2005), Lehmann discontinuity beneath North America: No
703 role for seismic anisotropy, *Geophys. Res. Lett.*, 32(9), doi: 10.1029/2004GL022333.

704

705 Vinnik, L., Kozlovskaya, E., Oreshin, S., & Kosarev, G. (2015), *Tectonophysics*, 667(23), 189-
706 198, doi: 10.1016/tecto.2015.11.024.

707

708 Wessel, P., & Smith, W.H.F. (1998), New, improved version of the Generic Mapping Tools
709 released, *Eos Trans. AGU*, 79, 579.

710

711 Whitcomb, J.H., & Anderson, D.L. (1970), Reflection of P'P' seismic waves from
712 discontinuities in the mantle, *J. Geophys. Res.*, 75(29), 5713-5728.

713

714 Wu, R.S., & Flatté, S. (1990), Transmission fluctuations across an array and heterogeneities in
715 the crust and upper mantle. *Pure Appl. Geophys.*, 132, 175-196.

716

717 Wu, R.S., & Xie, X. (1991), Numerical tests of stochastic tomography. *Phys. Earth Planet.*
718 *Inter.*, 67 (1991) 180-193.

719

720 Xu, W., Lithgow-Bertelloni, C., Stixurde, L., & Ritsema, J. (2008), The effect of bulk
721 composition and temperature on mantle seismic structure. *Earth. Planet. Sci. Lett.*, 275, 70-79.

722

723 Zhao, Y., Wu, Z., Wang, W., Deng, X., & Song, J. (2022), Elastic properties of Fe-bearing
724 Akimotoite at mantle conditions: Implications for composition and temperature in the lower
725 mantle transition zone, *Fundamental Research*, doi: 10.1016/j.fmre.2021.12.013.

726

727 Zheng, Y., & Wu, R.-S. (2008), Theory of transmission fluctuations in random media with
728 a depth dependent background velocity structure. *Adv. Geophys.*, 50, 21-41.

729

730

731

732

733

734

735

736

737

738

739